Progress in Additive Manufacturing
https://doi.org/10.1007/s40964-026-01851-0

RESEARCH

Effect of infrared nanosecond pulse laser polishing on surface quality, microstructure, and corrosion behaviour of additively manufactured Ti–6Al–4V alloy

Juan Ignacio Ahuir-Torres[1] · Guilherme Arthur Longhitano[2] · Geoff West[3] · Musa Bashir[4] · Hiren R. Kotadia[1]

Received: 21 January 2026 / Accepted: 6 July 2026

Abstract

Additive manufacturing (AM) enables the fabrication of complex Ti–6Al–4V components for biomedical applications, yet surfaces produced by electron beam powder bed fusion (EB-PBF) and laser-based powder bed fusion (LB-PBF) typically exhibit high roughness and surface defects that compromise corrosion performance. Conventional continuous-wave laser polishing can reduce their roughness, but it often induces microstructural changes that degrade the properties of AM alloys. This study demonstrates that infrared nanosecond-pulsed laser polishing provides an improved surface quality and corrosion resistance free of microstructural modification. EB-PBF and LB-PBF Ti–6Al–4V samples were polished using an infrared nanosecond pulsed laser and evaluated in terms of surface roughness, microstructure, and corrosion behaviour in simulated body fluid. Laser polishing reduced surface roughness by up to 38% for EB-PBF (from Sa ~ 40 to 25 µm) and 25% for LB-PBF (from Sa ~ 12 to 9 µm), while exhibiting a localised modification of the microstructure. Electrochemical testing revealed a significant increase in passive film breakdown potential ($\Delta E = 1.901–2.001$ V for EB-PBF and 1.800–1.900 V for LB-PBF), accompanied by a reduction in passive current density of approximately 85% for EB-PBF and 40% for LB-PBF. EB-PBF samples displayed the highest breakdown potential after polishing (2 V). Overall, nanosecond laser polishing is a promising method for improving the surface integrity and corrosion resistance of AM Ti–6Al–4V components for biomedical applications.

Keywords EB-PBF · LB-PBF · Nanosecond pulsed laser polishing · Corrosion · Ti–6Al–4V · Simulated body fluid · Additive manufacturing

✉ Juan Ignacio Ahuir-Torres
j.i.ahuirtorres@ljmu.ac.uk

✉ Hiren R. Kotadia
h.r.kotadia@ljmu.ac.uk

Guilherme Arthur Longhitano
guilonghita@gmail.com

Geoff West
G.West@warwick.ac.uk

Musa Bashir
M.B.Bashir@liverpool.ac.uk

[1] School of Engineering and Built environment, Liverpool John Moores University, Liverpool, UK

[2] Centro de Tecnologia da Informação Renato Archer, Campinas, Brazil

[3] WMG, University of Warwick, Coventry, UK

[4] Civil and Environmental Engineering, University of Liverpool, Liverpool, UK

1 Introduction

Metal additive manufacturing (AM) has transformed the production of patient-specific implants, offering unprecedented geometric freedom and the ability to fabricate complex structures directly from medical imaging data [1–3]. Among various AM technologies, laser powder bed fusion (LB-PBF) and Electron Beam Powder Bed Fusion (EB-PBF) have become the predominant processes for manufacturing biomedical components. Both techniques selectively melt thin layers of metal powder using a high-energy laser or electron beam, enabling the production of near-net-shape parts with mechanical properties comparable to conventionally processed Ti–6Al–4V [4].

Despite these advantages, powder-bed fusion technologies inherently produce rough, partially fused surfaces. Non-melted or sintered powder particles, staircase features

Published online: 23 July 2026

and melted track irregularities can significantly increase the surface roughness and introduce micro-porosity [5–8]. For biomedical implants, these defects are critical: surface roughness greater than a few micrometres reduces corrosion resistance, compromises passive-film stability, and can promote the release of powder particles into surrounding tissue, posing potential risks to patients [5]. Accordingly, standards such as ASTM F3335-20 emphasise the need for surface finishing to remove loosely adherent particles and sharp asperities.

However, post-processing AM implants remains challenging due to their complex geometry. Conventional mechanical or chemo-mechanical polishing often struggles to access internal channels or intricate lattice structures and can remove excessive material or introduce surface contaminants [9, 10]. Electrochemical approaches can reach recessed regions but risk altering surface chemistry or introducing residual electrolytes. These limitations motivate the development of highly controllable finishing methods compatible with complex AM geometries.

Laser polishing has emerged as a promising alternative due to its automation, environmental friendliness, selective processing capability, and absence of consumable abrasives [7, 9]. By rapidly melting a thin surface layer, laser-induced surface tension smooths asperities and consolidates the surface. Several methods exist, including continuous-wave (CW), pulsed, hybrid pulsed/CW and selective CW polishing, but each influences the underlying microstructure differently. Although CW lasers can yield extremely smooth surfaces, the prolonged melting duration often causes microstructural coarsening, grain growth or phase transformations that can degrade mechanical or corrosion performance [7]. In contrast, pulsed nanosecond lasers minimise heat-affected zone and produce much thinner re-melt layers, largely preserving the as-built microstructure because the thermal interaction time scales directly with pulse duration [11]. For Ti–6Al–4V manufactured by AM, nanosecond pulsed polishing has therefore become a compelling approach for achieving smoother surfaces while maintaining desirable $\alpha'/\alpha+\beta$ microstructures.

Despite extensive studies on laser polishing mechanisms [11–13], the specific influence of nanosecond pulsed polishing on the corrosion behaviour of Ti–6Al–4V fabricated by EB-PBF and LB-PBF remains insufficiently understood. Specifically, a systematic investigation of how AM techniques influence the corrosion response of samples subjected to nanosecond pulsed laser polishing remains a significant gap in the literature. Since corrosion resistance is fundamental to the long-term biocompatibility and durability of Ti–6Al–4V implants [6, 14–17], understanding how laser finishing modifies passive-film stability, charge-transfer kinetics, and electrochemical noise is essential.

The present work addresses this gap by thoroughly investigating the effect of 1064 nm, 200 ns pulsed-laser polishing on the microstructure, surface condition and corrosion response of Ti–6Al–4V manufactured using EB-PBF and LB-PBF. Corrosion behaviour was evaluated in simulated body fluid (SBF, 310 K, pH 7.4) using a combination of electrochemical noise analysis, potentiodynamic polarisation and electrochemical impedance spectroscopy. This study provides new insight into the process-surface-corrosion relationships governing laser-polished AM titanium alloys and contributes to the development of safer, more reliable additively manufactured implants.

2 Experimental methodology

2.1 Sample fabrication

The samples used in this study were fabricated using two different AM techniques: PBF-LB and PBF-EB. PBF-LB samples were cylinders with 7 mm diameter and 10 mm height, and PBF-EB were cylinders with 10 mm diameter and 25 mm height. Cylinders axes were aligned with the Z direction of the building platforms (building direction). LB-PBF samples were fabricated using Ti–6Al–4V commercial powder (EOS GmbH) with particle size between 20 and 80 µm in an EOSINT M270 (EOS GmbH) under argon (99.999% purity—White Martins) shielding atmosphere with oxygen control under 5 ppm. Build parameters were laser power of 170 W (Ytterbium fibre laser at 1070 nm wavelength from IPG Photonics), laser beam diameter of 100 µm, scanning speed of 1250 mm/s, layer thickness of 0.03 mm, and hatch spacing of 0.1 mm. After production, samples were removed from the building platform using electrical discharge machining. EB-PBF samples were fabricated using Ti–6Al–4V commercial powder (GE additive) with particle size between 45 and 100 µm in a Q10 plus (GE additive) under a vacuum atmosphere (under 5×10^{-4} mbar) with a continuous small He (99.999% purity—White Martins) injection. Build parameters were melting parameters, with hatch beam current maximum of 30 mA, hatch focus offset of 36 mA, external contour beam current maximum of 5 mA, hatch scanning speed of 4530 mm/s, external contour scanning speed of 750 mm/s, layer thickness of 0.05 mm, hatch spacing of 0.02 mm, plate temperature of 495 °C, and powder bed temperature of 940 °C. After production, samples were manually removed from the building platform, and loose sintered powder was removed using a GE additive powder recovery system.

Different powder particle size ranges were selected for LB-PBF and EB-PBF based on the distinct energy–matter interaction mechanisms associated with each process. In

LB-PBF, heat is generated through laser irradiation, where metals exhibit relatively high reflectivity and low absorption at the operating wavelengths [18]. As a result, finer powders are typically used to promote efficient melting, with particle sizes generally in the range of 15–45 µm [19], depending on the material and system. In contrast, EB-PBF generates heat through the kinetic energy of electron–powder interactions. Due to the charged nature of electrons, finer powders are more prone to electrostatic effects, which may lead to powder repulsion, "smoking," and beam deflection, affecting process stability [20]. Therefore, coarser powder particles, typically in the range of 45–106 µm, are used to minimise these effects [19]. Accordingly, the particle size distributions employed in this study were selected in line with the recommended ranges for each processing technique.

2.2 Laser processing

The laser polishing was conducted on the lateral surfaces of the cylindrical samples, which, compared to the top surfaces, present higher roughness and complexity [21]. The laser processing was carried out using a laser system formed of an infrared (1064 nm) nanosecond (200 ns) pulsed laser, an optical system, and a galvanometer mirror scanner, which is detailed in previous work [22]. The laser parameters were selected to optimise the average surface roughness (S_a) and eliminate micropores for each sample type (EB-PBF and LB-PBF) (Table 1). Although the application of the multi-passes in the polishing processes can yield a slight increase in the reduction in S_a associated with the increase in melt-pool dimensions [23], this application can also promote the crack formation and the material ablation, thereby inducing material deterioration [24]. Consequently, the single-pass methodology was adopted for the laser polishing process to mitigate these detrimental defects. It is noteworthy that the laser beam diameter and scan overlap employed for laser polishing varied as a function of manufacturing technique, consistent with the observed differences in S_a generated between the two process (40 ± 4 µm for EB-PBF and 12 ± 1 µm for LB-PBF).

Table 1 Selected laser polishing parameters for EB-PBF and LB-PBF samples

Parameter	Manufacturing method	
	Electron beam	Laser beam
Model	SPI Laser (UK) G3 20 W nanosecond pulsed fibre laser	
Pulse length (ns)	200	
Maximum power of the laser (W)	22	
Power employed (W)	15	
Pulse frequency (kHz)	25	
Pulse energy (µJ)	617	
Scan speed (mm/s)	30	
Atmosphere	Argon 99.999% purity and 3 Bar pressure	
Distance from the focal point (µm)	0	400
Rayleigh length (µm)	898	
Laser beam diameter (µm)	51	70
Energy fluence (J cm^{-2})	58	32
Energy density (J mm^{-2})	10	7
Peak power density (MW cm^{-2})	250	150
Line overlap area (%)	98	
Pulse-to-pulse overlap	42	58
Thermal diffusion length (nm)	836	
Scan overlap (%)	25	50

Laser beam diameter (D_o) and energy density (E_d) were calculated through Eq. (1) [25] and Eq. (2) [26], respectively.

$$D_o = d_o\sqrt{1+\left(\frac{Z^2}{R_L^2}\right)} \tag{1}$$

$$E_d = \frac{4E_p}{\pi D_o^2 \tau} \tag{2}$$

where d_o is the focused laser beam diameter, R_L is the Rayleigh length, Z is the distance from the focal point, E_p is the pulse energy, τ is the pulse length.

Notably, the laser polishing was conducted in a shielding atmosphere (argon supplied by BOC) using an in-house inert chamber. The laser-polished samples were designated as "EB-PBF + laser polishing" and "LB-PBF + laser polishing" for the samples produced by electron beam and laser additive manufacturing, respectively.

2.3 Corrosion analysis

The electrochemical trials were conducted using a potentio/galvanostat (Interface1010E, Gamry Instruments Inc). The potentio/galvanostat was controlled via *Gamry Framework* software and the electrochemical data were assessed using *Gamry Echem Analyst* software. All electrochemical testing was made using a three-electrode cell (Reference, counter, and working electrode). The reference electrode was a 3M KCl silver/silver chloride (Ag/AgCl 3M KCl) of double junction (EDT direct ion Ltd). The counter-working electrode was a platinum wire of 0.7 mm diameter (Heimerle + Meule Group). The working electrodes were the samples. The electrochemical trials were conducted in simulated body fluid (SBF) at 310 K and 7.4 pH (Table 2 [14–16]). The temperature was maintained using a hotplate (Stuart, SB162 provided by BioCote). pH was measured with a pHmeter (Jenway 350pH Meter supplied by Scientific Laboratory Supplies) and adjusted with 1 M HCl and 1 M NaOH. All chemical agents were provided by Merck-Sigma-Aldrich.

Table 2 Chemical composition of SBF in g/L [14–16]

Chemical compound	Quantity (g/L distilled water)
NaCl	8.035
$NaHCO_3$	0.355
KCl	0.225
$K_2HPO_4 \cdot 3H_2O$	0.231
$MgCl_2 \cdot H_2O$	0.311
$CaCl_2 \cdot H_2O$	0.292
Na_2SO_4	0.072
$(CH_2OH)_3(CNH_2)$	6.118
pH	7.4

Prior to and after the corrosion testing, the samples were cleaned using commercial detergent and fresh water, then distilled water soaking, and finally, isopropanol spraying. The exposed area of the samples (working electrode) was set with a hole generator on an electrical insulation tape. The rims of the hole were sealed with epoxy resin to avoid crevices and leaks. The consumables and tools were provided by RS components.

The electrochemical trials were asymmetric electrochemical noise (AEN), potentiodynamic polarisation curve (PPC), and electrochemical impedance spectroscopy (EIS). AEN combined open circuit potential (OCP) with zero resistance ammeter (ZRA) techniques at the same time. AENs were conducted for 3600 s with 0.05 s of the acquisition time, resulting in a total of 72,000 measurements. PPC testing was carried out with an initial potential of − 0.3 V versus OCP after 1 h immersion in SBF at 310 K and 7.4 pH, with a voltage scan rate of 0.167 mV s^{-1}, the inverting current was 500 µAcm^{-2}, and the inverting potential was 3 V versus Ag/AgCl 3M KCl. EIS were set at 10 mV root mean square potential amplitude, frequency range from 10^{-2} to 10^5 Hz with 10 points per frequency decade. EIS studies were conducted at 1 h of immersion time in SBF to analyse the corrosion mechanisms.

Noteworthy that all electrochemical testing was repeated at least three times to confirm the veracity of the results.

2.4 Material characterisation

The pre- and post-corroded (after PPC) surface, as well as the cross-section of the samples, were examined using a scanning electron microscope (SEM) (TM4000 Plus Tabletop SEM series, Hitachi), working with backscattered electrons (BSE), 15 kV potential acceleration, 70 µA current tension, and 2 µm spot size. The cross-section preparation followed a metallographic process involving a polishing process and a subsequent etching. The cross-sections were initially polished with SiC abrasive papers of P400 grit and P2400 grit, followed by a final mirror-to-polishing with a 50% in volume of distilled water colloidal silica gel dissolution with 40 nm of grain size. The polishing consumables and equipment were provided by Struer Ltd. For etching, the cross-sections of the samples were treated with a dissolution consisting of 93% distilled water, 6% HNO_3, and 1% HF by volume for 30 s. All chemical agents were supplied by Merck-Sigma-Aldrich. The chemical composition of the pre- and post-corroded samples was assessed using energy dispersive spectroscopy (EDS) mapping and was identical to that used for SEM, except for a 3 µm spot size. S_a of the samples were measured with a digital optical microscope (VHX-X1, Keyence) using 500X magnification with coaxial light and 1 µm pitch. Measurements were processed with a Gaussian filter.

3 Results and discussion

3.1 Materials analysis

Figure 1 presents the surface and cross-sectional morphologies of the Ti–6Al–4V samples produced by EB-PBF and LB-PBF, before and after nanosecond laser polishing. The as-built surfaces (Fig. 1a, c) exhibit the characteristic spherical partially melted powder particles commonly reported in powder bed fusion systems [27, 28]. Their presence reflects both the layer-wise process and the incomplete consolidation of peripheral powder. Consistent with the particle size distributions of the feedstock materials, the electron beam surfaces contain noticeably larger adhered particles (45–100 µm), whereas laser beam surfaces display finer particles (20–80 µm). It should be noted that the as-built surfaces were not subjected to any pre-treatment, including additional polishing.

After laser polishing, these adhered spheres are fully removed (Fig. 1b, d), confirming that the pulsed laser process effectively melts and redistributes the superficial asperities, as also observed in prior studies [7, 12, 29, 30]. Small depressions observed on the polished surfaces correspond to opened subsurface pores. Their formation is attributed to melt-pool hydrodynamics: when the top layer is locally melted, internal pore pressure drives liquid displacement outward, causing pore exposure upon resolidification [12, 30]. This mechanism is typical when nanosecond pulses reshape the surface via rapid local melting–solidification cycles. Localised ablations can be as a result of the inherent material removal mechanisms associated with the laser–material interaction.

The cross-sectional images further reveal distinct microstructures associated with each AM process. EB-PBF samples exhibit the expected α/α′ lamellar morphology with retained β between lamellae. This is consistent with the high build-plate temperatures and lower thermal gradients characteristic of EB-PBF, which promote diffusion and

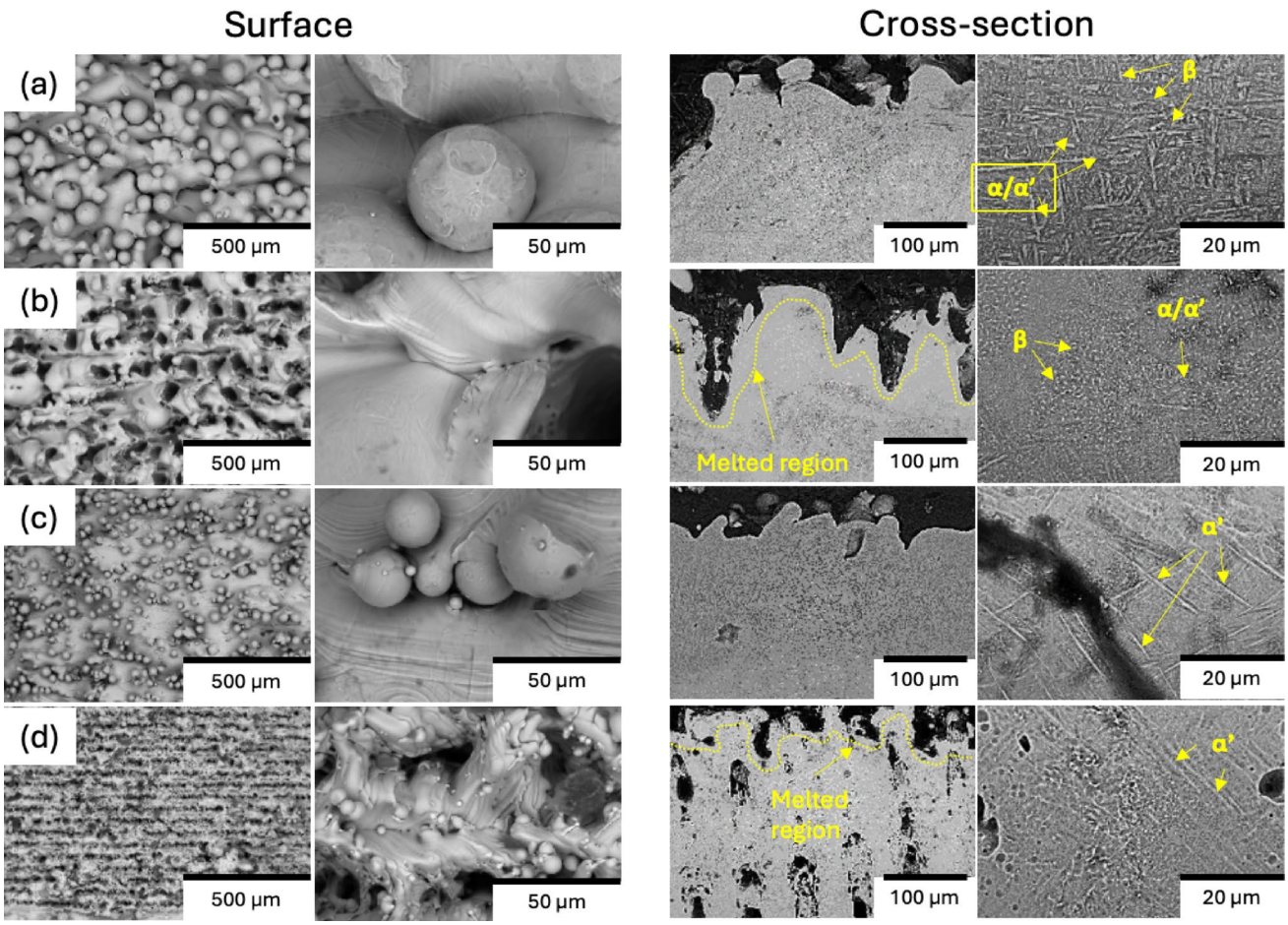

Fig. 1 SEM (BSE) images showing surface and cross-sectional morphology of Ti–6Al–4V fabricated by **a** EB-PBF, **b** EB-PBF + laser polishing, **c** LB-PBF, and **d** LB-PBF + laser polishing

lamellar coarsening [17]. In contrast, LB-PBF contain predominantly α′ martensite, formed due to the extremely high cooling rates ($>10^3$ K/s) characteristic of laser-based processes [31]. These observations align with the established process–microstructure relationships for Ti–6Al–4V across PBF methods [12, 27, 28].

Laser polishing produces different microstructural responses depending on the initial surface condition. For EB-PBF, a refinement of the near-surface microstructure is observed. EB-PBF surfaces are considerably rougher, causing multiple reflections and backscattering of the incident laser beam [22, 32]. This effectively enlarges the melt-pool diameter, increasing the total resolidification time. Since α/β phase morphology strongly depends on thermal gradients and cooling rates, the extended resolidification time results in partial refinement of the α/α′ lamellae [23, 33, 34]. By contrast, LB-PBF surfaces, which begin with lower roughness, do not produce the same degree of beam spreading; therefore, their polished microstructure remains largely α′-dominated and resembles the as-built condition.

It is noteworthy that the melt depth was comparable for both additively manufactured samples (10 ± 1 µm), which is attributed to the use of a nanosecond pulsed laser. In short-pulse laser processing, the thermal diffusion length is primarily governed by the pulse duration [35, 36]. Based on the measured melt depth and the observed localised ablation features, the laser polishing process in the present study can be classified as surface over melting (SOM) [37, 38].

Grain orientation mapping (Fig. 2) highlights further differences in solidification behaviour between the two AM processes. EB-PBF samples (Fig. 2a) show large, domain-like regions with consistent grain orientation, indicative of low cooling rates and spatially heterogeneous thermal fields [39]. LB-PBF samples (Fig. 2b) instead display more homogeneous grain distributions, consistent with rapid and directionally uniform heat extraction during laser melting [40]. Laser polishing modifies the grain orientations only locally; while some refinement is observed, the underlying texture remains dominant. As a result, EB-PBF + polished samples (Fig. 2c) retain their more heterogeneous grain orientation patterns, whereas LB-PBF + polished samples (Fig. 2d)

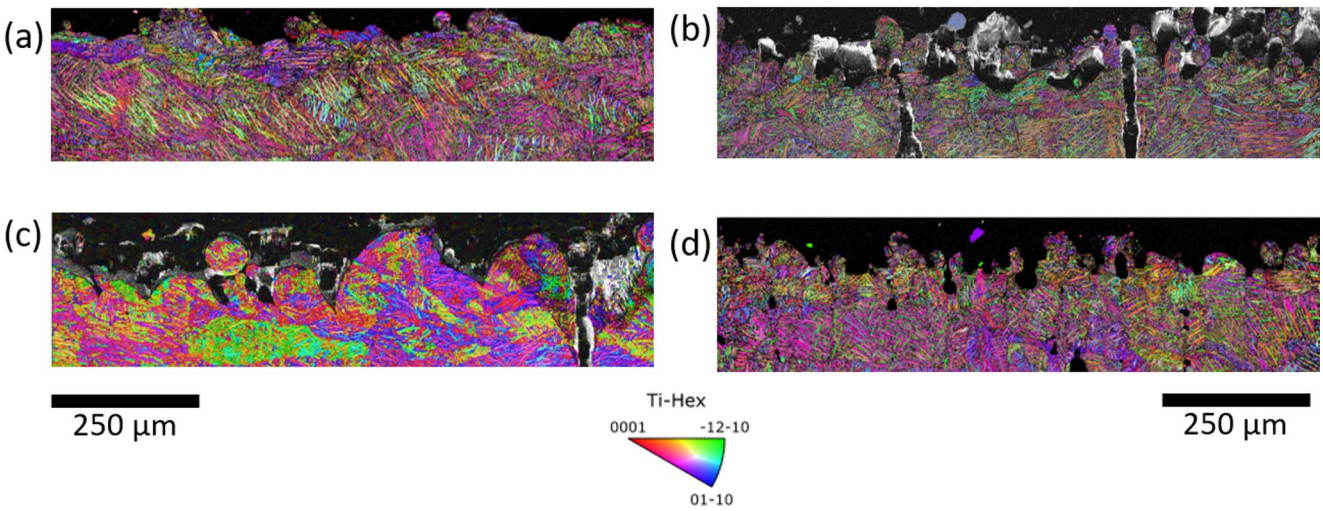

Fig. 2 EBSD inverse pole figure (IPF-Z) maps of cross-sections for Ti–6Al–4V manufactured by **a** EB-PBF, **b** EB-PBF + laser polishing, **c** LB-PBF, and **d** LB-PBF + laser polishing. EB-PBF samples show heterogeneous grain orientation domains caused by lower cooling rates and non-uniform thermal gradients, while LB-PBF samples exhibit more homogeneous grain orientation with a preferred <0001> texture. Laser polishing induces only superficial refinement, with the bulk solidification texture largely preserved in both manufacturing routes

maintain a stronger <0001> preferential orientation. These trends confirm that single-pass nanosecond polishing does not induce full recrystallisation but rather affects only the superficial thermally cycled material.

As-built surfaces exhibit partially melted powder particles characteristic of PBF processes, with larger adhered particles in EB-PBF due to its coarser feedstock. Laser polishing removes these adhered particles and exposes sub-surface pores through melt reflow. Cross-sectional images reveal the α/α′ lamellar microstructure for EB-PBF samples and α′ martensitic structure for LB-PBF samples, with local refinement in EB-PBF samples after polishing due to extended resolidification times. In particular, cross-sectional EBSD analysis reveals the presence of a remelted surface layer with an estimated thickness of ~ 10 µm, within which a localised refinement of the α/α′ lamellar structure is observed in EB-PBF samples. An increased density of surface-connected defects and pore exposure is evident following laser polishing. These microstructural modifications are expected to influence corrosion behaviour by: Promoting a more homogeneous passive film formation within the refined layer, reducing localised stress concentration sites, and altering diffusion pathways at the surface.

EBSD cross-sections represent a highly localised 2D section of the material and may not capture the full three-dimensional pore distribution, particularly for small or subsurface porosity typical of additively manufactured Ti–6Al–4V. Therefore, the apparent low pore density in Fig. 2 does not necessarily indicate the absence of internal pores.

Surface chemical analysis (Fig. 3) also shows that elemental distributions remain largely unchanged after polishing, demonstrating that the process does not introduce significant chemical modification. The argon shielding atmosphere effectively minimises thermal oxidation during pulsed laser exposure [27, 28]. The oxygen detected originates from passive TiO_2 film formation, which naturally develops upon exposure to air. Localised aluminium-rich regions are observed on both polished and unpolished surfaces. This observation can be attributed to the considerably lower boiling point of aluminium (2470 K) relative to Ti (3560 K) and V (3407 K). Under transient high-temperature conditions during AM or polishing, selective Al evaporation occurs; once condensed, Al can redeposit on the surface.

EB-PBF samples display substantially higher S_a values than LB-PBF samples (Fig. 4), consistent with the larger feedstock particle size, thicker layers, and higher preheat temperatures used in EB-PBF. Following polishing, S_a reduces markedly for both manufacturing routes. This reduction results from melt-pool reflow, remelting of adhered powder, and sealing of small surface pores, all characteristic of nanosecond pulsed laser polishing [12, 29, 30]. While surface roughness is often linked to improved osseointegration, excessive roughness increases bacterial adhesion and significantly reduces corrosion resistance [41]. Therefore, achieving controlled roughness reduction through laser polishing is particularly attractive for biomedical applications, balancing biocompatibility requirements with electrochemical stability.

As previously mentioned, the additively manufactured samples presented high roughness values. In EB-PBF, a larger mean particle size as well as higher layer thickness leads to higher S_a values, when compared to the LB-PBF samples. For the polished samples, the nanosecond pulse laser process reduced S_a for both conditions (Fig. 4), as an

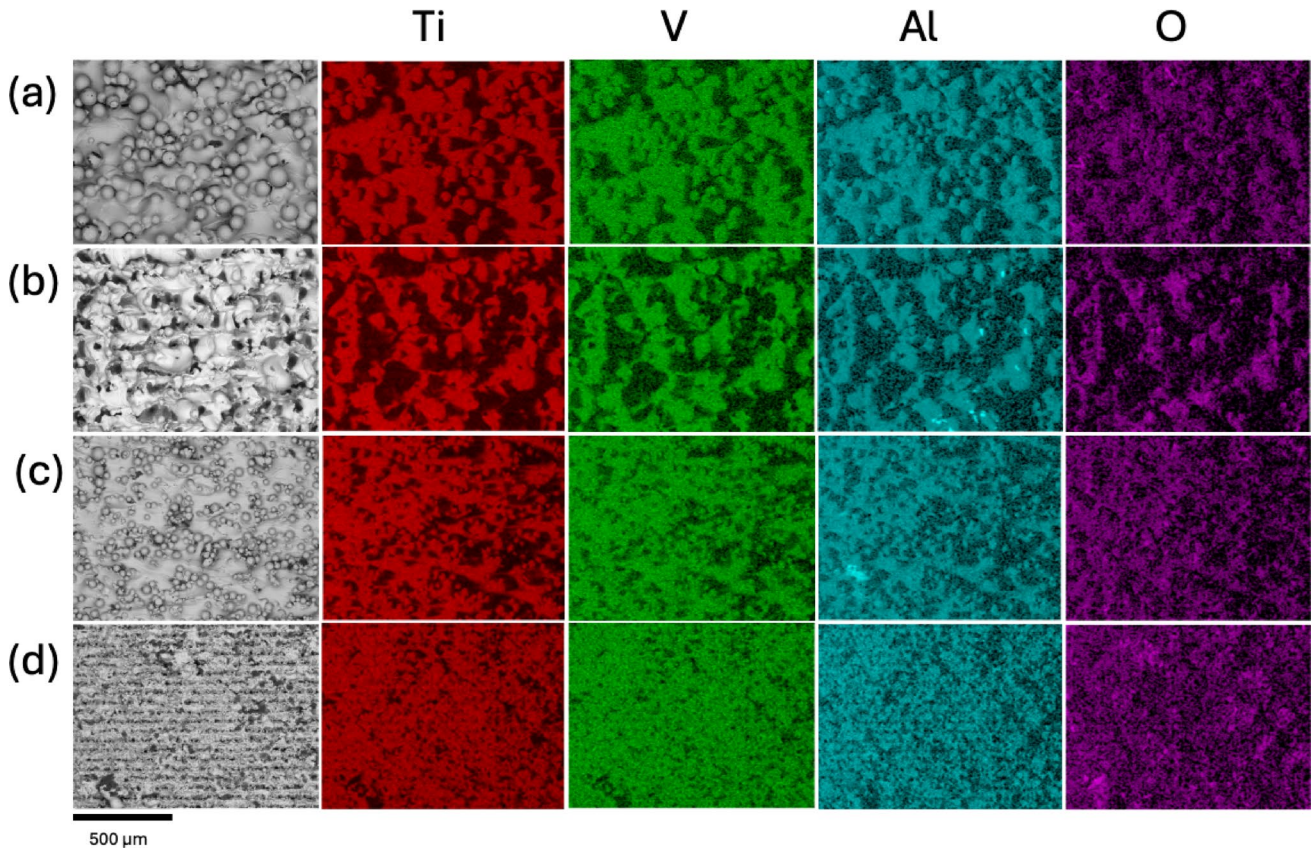

Fig. 3 EDS mapping analyses of the **a** EB-PBF, **b** EB-PBF + laser polishing, **c** LB-PBF, and **d** LB-PBF + laser polishing

effect of powder remelting and pores sealing [12, 29, 30]. In biomedical applications, roughness plays an important role in cell adhesion, proliferation, and differentiation [42], as well as in bacterial adhesion [41]. In this regard, laser polishing can be a notorious tool for roughness modification of biomedical parts. The laser-polished samples exhibited Sa values of 24 ± 2 µm (EB-PBF + laser polishing) and 10 ± 1 µm (LB-PBF + laser polishing), both of which lie within the optimal range for osseointegration applications [43].

3.2 Electrochemical analyses

3.2.1 AEN analyses

The electrochemical behaviour of the samples in SBF was first assessed through asymmetric electrochemical noise (AEN), which provides insight into metastable corrosion activity without externally perturbing the system. The potential and current density temporal evolution (Fig. 5) shows that all samples exhibited fluctuations around relatively steady baseline values. Such fluctuations are characteristic of passive metals undergoing local breakdown and rapid repassivation, and are consistent with the passive film dynamics expected for Ti–6Al–4V in chloride-containing physiological environments. The fluctuations arise from metastable micropitting, where chloride ions locally penetrate the passive TiO_2 layer, producing momentary depassivation. This causes a rapid increase in current density (Fig. 5b) and a corresponding drop in potential (Fig. 5a). As the underlying Ti oxidises, the passive film is restored and both potential and current stabilise again [44, 45]. Although this behaviour occurs in all samples, its magnitude and frequency differ according to surface condition and manufacturing route, reflecting the microstructural and topographical differences described in Sect. 3.1.

The quantitative corrosion parameters derived from AEN (OCP and ZRA) (Table 3) further illustrate the influence of AM route and laser polishing on corrosion kinetics. The noise-derived corrosion rate ($C.R._{AEN}$) [46] and the noise resistance (R_{AEN}) [47, 48] were calculated using established expressions. These parameters quantify the corrosion kinetics of the passive film.

$$C.R._{AEN} = \frac{I_{R.M.S} \times M}{n \times F \times d} \tag{2}$$

$$R_{AEN} = \frac{\sigma_E}{\sigma_I} \tag{3}$$

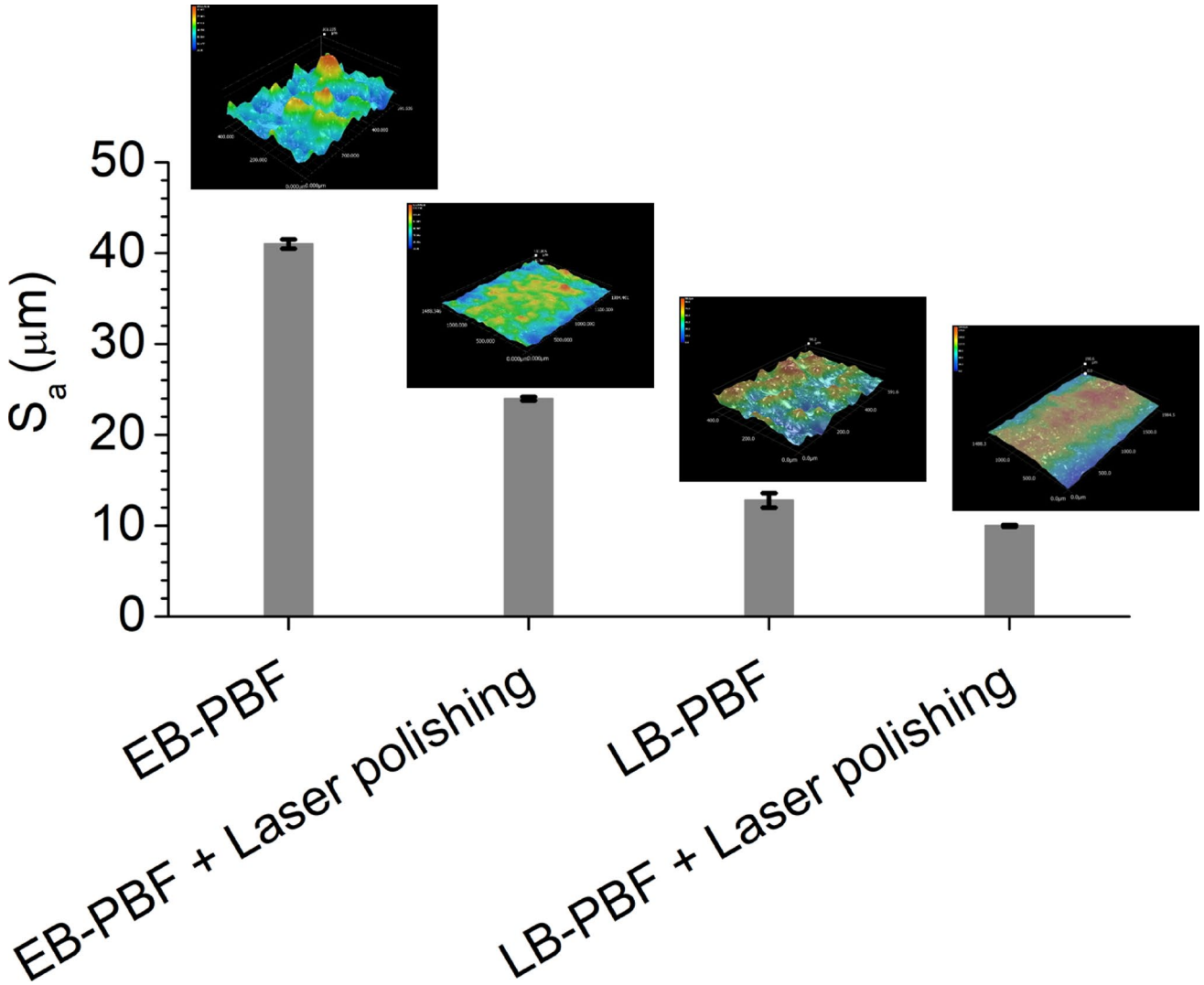

Fig. 4 S_a of the additively manufactured Ti–6Al–4V alloy as-built and laser-polished samples

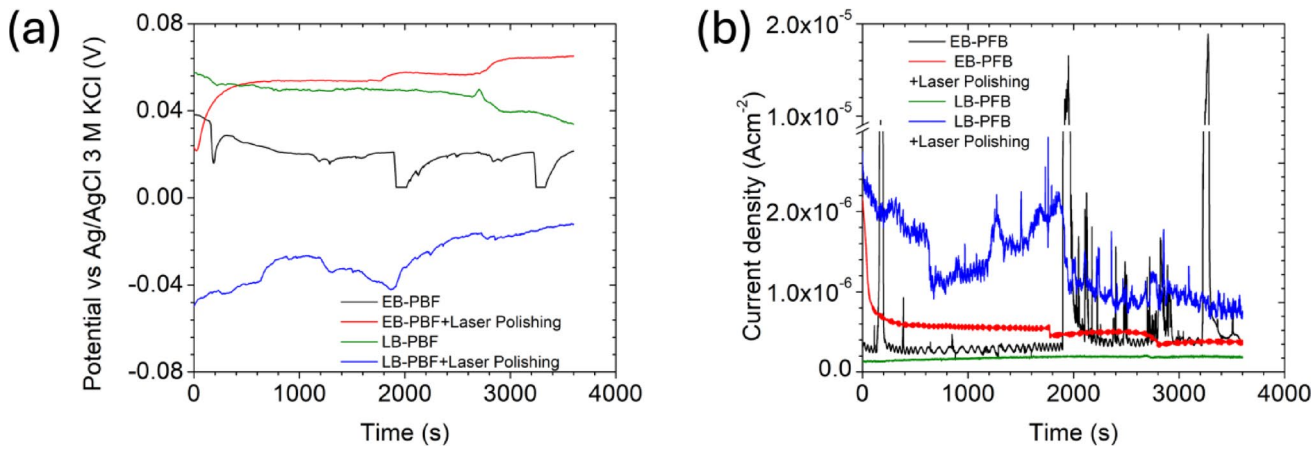

Fig. 5 Asymmetric electrochemical noise data for Ti–6Al–4V in SBF (310 K, pH 7.4): **a** OCP showing metastable passivity breakdown events; **b** ZRA current showing transient pit initiation and repassivation

Table 3 Corrosion parameters derived from AEN

Sample	$I_{R.M.S}$ (A cm^{-2}) (10^{-7})	σ_I (A cm^{-2}) (10^{-7})	$C.R._{AEN}$ (μm year^{-1})	$L.I$	σ_E (mV)	R_{AEN} (kΩ cm^2)
EB-PBF	1.771 ± 0.005	5.102 ± 0.004	1.575 ± 0.005	2.88 ± 0.02	5.590 ± 0.002	10.956 ± 0.007
EB-PBF + laser polishing	6.023 ± 0.007	0.196 ± 0.003	5.357 ± 0.007	0.03 ± 0.01	7.212 ± 0.004	368.335 ± 0.009
LB-PBF	2.728 ± 0.003	1.677 ± 0.008	2.426 ± 0.006	0.61 ± 0.05	5.219 ± 0.003	31.121 ± 0.003
LB-PBF + laser polishing	9.655 ± 0.006	3.798 ± 0.005	8.587 ± 0.009	0.39 ± 0.03	9.887 ± 0.009	26.030 ± 0.007

Here, $I_{R.M.S}$ is the current density root mean square, M is the molar mass of the titanium (47.9 g mol^{-1}), n electron number transferred in the corrosion reaction (4), F is the Faraday constant (96,500 C mol^{-1}), d is the Ti–6Al–4V density (4.4 g cm^{-3}), σ_E and σ_I were the standard deviation of the potential and current density. $I_{R.M.S}$, σ_E and σ_I were calculated utilising Eqs. (4), (5), and (6), respectively.

$$I_{R.M.S} = \sqrt{\frac{1}{N}\sum_{i=1}^{N} I_i^2} \tag{4}$$

$$\sigma_I = \sqrt{\frac{\sum_{i=0}^{N} \left(I_i - \bar{I}\right)^2}{N-1}} \tag{5}$$

$$\sigma_E = \sqrt{\frac{\sum_{i=0}^{N} \left(E_i - \bar{E}\right)^2}{N-1}} \tag{6}$$

Here, N is the number of the measurements, I_i and E_i are the values of each current density and potential measurements, respectively, $\bar{I}$ and $\bar{E}$ are the average values of the current density and potential, correlatively.

All samples showed very low $C.R._{AEN}$ values (μm year^{-1} scale), confirming that Ti–6Al–4V maintains excellent corrosion resistance under physiological conditions. However, trends reflect clear structure–property relationships: (i) EB-PBF samples exhibited the highest noise activity (lower R_{AEN}), consistent with their rough surface and partially fused particles, and (ii) EB-PBF + Laser polishing samples showed a dramatic increase in R_{AEN}, demonstrating a more stable passive film after polishing. LB-PBF samples showed less drastic changes, consistent with their lower initial roughness. Thus, laser polishing enhances corrosion stability chiefly through surface smoothening and removal of defect sites.

Localised Corrosion Index ($L.I.$) derived from ZRA data and Eq. (7) [47], provides insight into whether corrosion is predominantly uniform or localised.

$$L.I. = \frac{\sigma_I}{I_{R.M.S}} \tag{7}$$

Most samples exhibited $L.I.$ values between 0.4 and 0.7, indicating a mixed corrosion mode-uniform dissolution punctuated by metastable pitting. The exception was the EB-PBF sample, which presented: $L.I. = 2.88$ to strongly localised corrosion. This behaviour aligns with the morphological features described earlier: high roughness, interparticle voids and crevice-like features enhance localised attack [49]. Laser polishing reduced L.I. to nearly zero, confirming that surface modification directly mitigates roughness-driven localised corrosion. These findings provide a systematic identification of the corrosion mechanisms and properties of laser non-polished and polished additively manufactured Ti6Al4V (EB-PBF and LB-PBF) under non-perturbative conditions.

When combined with the microstructural and topographical observations from Sect. 3.1, the AEN results clearly demonstrate the governing role of surface condition and melt-pool–driven microstructural features on the corrosion behaviour of AM Ti–6Al–4V. EB-PBF samples, characterised by larger powder particles, a coarse α/α′ lamellar microstructure, and significantly higher roughness, showed the most pronounced corrosion activity and the highest tendency towards localised attack. The abundance of partially fused particles and open pore features provides favourable sites for chloride-induced passive film rupture, explaining the elevated fluctuation amplitudes of the signals and the high $L.I$ value observed. Application of nanosecond pulsed laser polishing markedly stabilised the corrosion response, primarily through the removal of loosely bonded particles, reduction of asperities, and modification or sealing of surface-connected porosity. For the electron beam, the rougher initial surface also promoted greater beam scattering and larger effective melt-pool dimensions, leading to slower cooling and refining of the near-surface microstructure, further contributing to improved passivity.

In contrast, LB-PBF samples, which naturally exhibit smoother surfaces and finer α′ martensitic structures due to higher cooling rates during fabrication, displayed intrinsically better passive film stability. Nevertheless, laser polishing still produced modest improvements in AEN-derived parameters, indicating subtle enhancements in passive film uniformity and reduction of metastable breakdown events. Collectively, the electrochemical and microstructural evidence confirms that early-stage corrosion behaviour in simulated body fluid is dominated by the surface state, and that nanosecond pulsed laser polishing provides an effective and

non-contact route to enhance the electrochemical stability of both EB-PBF and LB-PBF Ti–6Al–4V.

3.2.2 Potentiodynamic polarisation curve assessments

The potentiodynamic polarisation curves for all samples are shown in Fig. 6. The cathodic branches were similar across all conditions, displaying the characteristic sloped behaviour associated with activation-controlled oxygen reduction in SBF, consistent with previous studies on Ti–6Al–4V in chloride-containing environments [16, 50]. In the anodic branches, all samples exhibited a nearly constant current density with an increase in potential until a certain voltage, according to the type of sample. This behaviour is indicative of the passive film presence, which is typical in titanium alloys. The voltage region of the passive film further displayed fluctuations in current density as the potential increased. These oscillations correspond to metastable micropitting events, where chloride ions locally disrupt the passive TiO_2-based film, followed by rapid repassivation, as previously described in Sect. 3.2.1 [16, 45, 51]. At higher potentials, all curves showed a sharp rise in current density, marking the passive film breakdown potential (E_{bp}), a key indicator of the thermodynamic stability of the passive layer [17, 50]. Importantly, the return scan for each condition rejoined the forward curve at potentials substantially above corrosion potential (E_{corr}), confirming that all samples retained the ability to spontaneously repassivate, even after passive-film breakdown, an essential property for biomedical implant alloys.

The potentiodynamic response revealed distinct differences between the anodic behaviour of polished and unpolished samples. For both EB-PBF and LB-PBF conditions, the unpolished surfaces exhibited a gradually rising anodic branch from E_{corr} to E_{bp}. This inclined profile reflects continuous passive-film evolution with increasing potential, driven by the presence of surface asperities, partially fused particles, and micro-crevices that promote localised chemical activation and passive-film transformation. In contrast, the laser-polished samples showed an almost vertical anodic branch, indicating a far more stable passive film across the same potential range [52]. This stability is attributed to the removal of adhered particles, the reduction or sealing of micro-crevices, and the overall smoothing of the near-surface microstructure. Additionally, the crystallographic texture plays a critical role: laser beam samples, which exhibit a higher fraction of (0001) orientations, form passive films with intrinsically lower electron-transfer rates and therefore enhanced stability [53]. Collectively, these effects show that laser polishing not only modifies surface topography but also strengthens the thermodynamic robustness of the passive film.

Quantitative PPC parameters for all conditions are summarised in Table 4. Although E_{corr} values broadly followed the same trends observed in the AEN analysis, the passive film breakdown potential (E_{bp}) provides a more reliable indicator of thermodynamic stability for passive alloys such as Ti–6Al–4V [50]. Across both manufacturing routes, laser polishing produced a clear increase in E_{bp}, demonstrating an improved ability of the surface oxide to withstand higher anodic potentials before breakdown. The

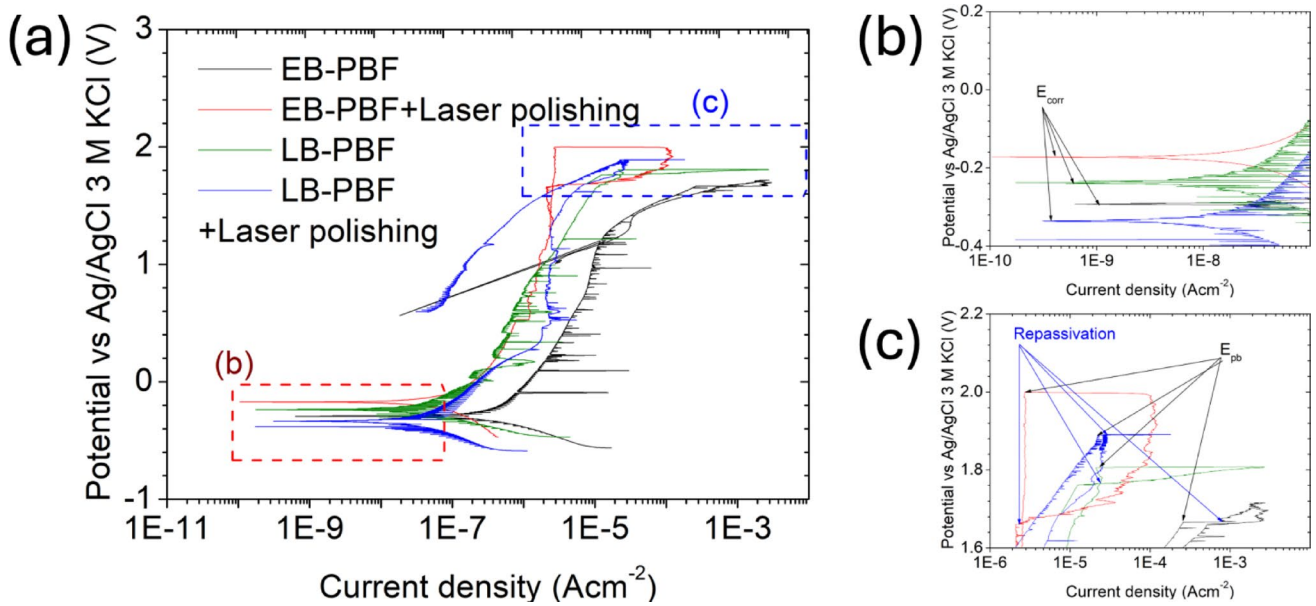

Fig. 6 Potentiodynamic polarization curves (PPC) for the samples in SBF at 310 K and 7.4 pH. **a** Overall PPC curves and zoom in **b** E_{corr} and **c** E_{bp} regions

Table 4 Thermodynamic and kinetic characteristics of the samples in SBF at 310 K and 7.4 pH obtained using PPC

Sample	E_{corr} (V)	E_{bp} (V)	I_{corr} (A cm^{-2})	β_c	β_a	I_{pass} (A cm^{-2})	$C.R._{pass}$ (µm year^{-1})
EB-PBF	− 0.239 ± 0.002	1.661 ± 0.004	1.451 10^{-7} ± 0.005 10^{-7}	0.049 ± 0.002	0.066 ± 0.005	8.090 10^{-6} ± 0.005 10^{-6}	72 ± 1
EB-PBF + laser polishing	− 0.173 ± 0.005	2.001 ± 0.005	3.280 10^{-8} ± 0.003 10^{-8}	0.072 ± 0.005	0.075 ± 0.006	1.198 10^{-6} ± 0.003 10^{-6}	11 ± 1
LB-PBF	− 0.238 ± 0.008	1.800 ± 0.005	1.966 10^{-8} ± 0.006 10^{-8}	0.015 ± 0.001	0.016 ± 0.001	2.830 10^{-6} ± 0.008 10^{-6}	25 ± 2
LB-PBF + laser polishing	− 0.332 ± 0.009	1.900 ± 0.003	1.512 10^{-9} ± 0.007 10^{-9}	0.020 ± 0.002	0.031 ± 0.002	1.690 10^{-6} ± 0.007 10^{-6}	15 ± 1

EB-PBF + polishing samples exhibited the most pronounced improvement in E_{bp}. This enhancement can be attributed to several synergistic effects: (i) reduction of micropores and crevices that would otherwise produce locally thin passive films [54, 55], (ii) refinement of the near-surface microstructure caused by extended melt-pool solidification during polishing [53], as discussed in Sect. 3.1, and (iii) homogenisation of grain orientations, which promotes the formation of passive film with more uniform thickness and composition [53]. Conversely, the smaller improvement observed for LB-PBF + polishing aligns with their inherently smoother as-built surfaces and limited microstructural modification during polishing. Consequently, the thermodynamic benefit of laser processing is largest where the surface initial condition is most heterogeneous [6, 55].

For passive alloys, the passive current density (I_{pass}), rather than the corrosion current density (I_{corr}), more accurately reflects corrosion kinetics, as it represents the steady-state current associated with passive-film dissolution and repair [50]. The passive corrosion rate ($C.R._{pass}$) was calculated using Eq. (8) [46]:

$$C.R._{pass} = \frac{I_{pass} \times M}{n \times F \times d} \tag{8}$$

where M is the molar mass of Ti (47.9 g mol^{-1}), n=4 is the number of electrons exchanged, F is Faraday's constant (96,500 C mol^{-1}), and d is the density of Ti–6Al–4V (4.4 g cm^{-3}).

The kinetic trends further highlight the influence of manufacturing route and surface condition: EB-PBF samples exhibited the highest $C.R._{pass}$, consistent with their rougher surfaces, lamellar α/α′ microstructures, and less favourable crystallographic texture. LB-PBF samples showed inherently lower $C.R._{pass}$, which is attributed to smoother surfaces, finer microstructures, and the prevalence of (0001)-oriented grains known to impede electron transfer across the passive film–metal interface [56, 57]. Laser polishing significantly decreased $C.R._{pass}$ for both EB-PBF and LB-PBF samples. This improvement stems from: (i) the reduction or elimination of crevices and pores that locally accelerate corrosion, (ii) the decrease in true surface area exposed to the electrolyte due to lower roughness, and (iii) a more uniform passive film resulting from microstructural smoothing. Notably, the EB-PBF + polishing sample showed the largest decrease in $C.R._{pass}$, mirroring the substantial surface and microstructural changes induced by the polishing process (Sect. 3.1). This confirms that the benefit of nanosecond laser polishing is greatest for samples with initially high levels of surface heterogeneity. Notably, the $C.R._{pass}$ trend was inconsistent with the $C.R._{AEN}$ behaviour (Sect. 3.2.1), reflecting inherent electrochemical differences between the two techniques. These discrepancies can be attributed to the AEN technique predominantly capturing features associated with cathodic reactions, whereas PPC enables the assessment of both anodic and cathodic processes [58, 59]. These findings provides the first systematic investigation of the effect of laser polishing on the thermodynamic and kinetic corrosion resistance of components manufactured by EB-PBF and LB-PBF.

3.2.3 Electrochemical impedance spectroscopy evaluation

The corrosion behaviour of the samples was further assessed using Electrochemical Impedance Spectroscopy (EIS), presented as Nyquist and Bode plots in Fig. 7. All samples showed broadly similar electrochemical responses, characterised by an equivalent circuit containing four distinguishable time constants, indicating comparable corrosion mechanisms across manufacturing and polishing conditions.

At high frequency (10^4–10^5 Hz), the impedance modulus exhibited a plateau, indicating a pure resistive response associated with the solution or electrolyte resistance (R_s) [60, 61]. As expected, R_s was similar for all samples (≈7–9 Ω cm^2), since this parameter depends primarily on solution conductivity rather than surface condition [15, 51].

The second time constant was identified from the depressed semicircle in the Nyquist plot and from a peak in both modulus and phase angle in the medium-frequency region (10^2–10^3 Hz). This feature was modelled as a constant phase element (CPE) in parallel with a resistance and represents the electrochemical response of the passive oxide film (CPE_{film} and R_{film}) [33, 52, 62]. The CPE describes the non-ideal capacitive behaviour associated with interfacial

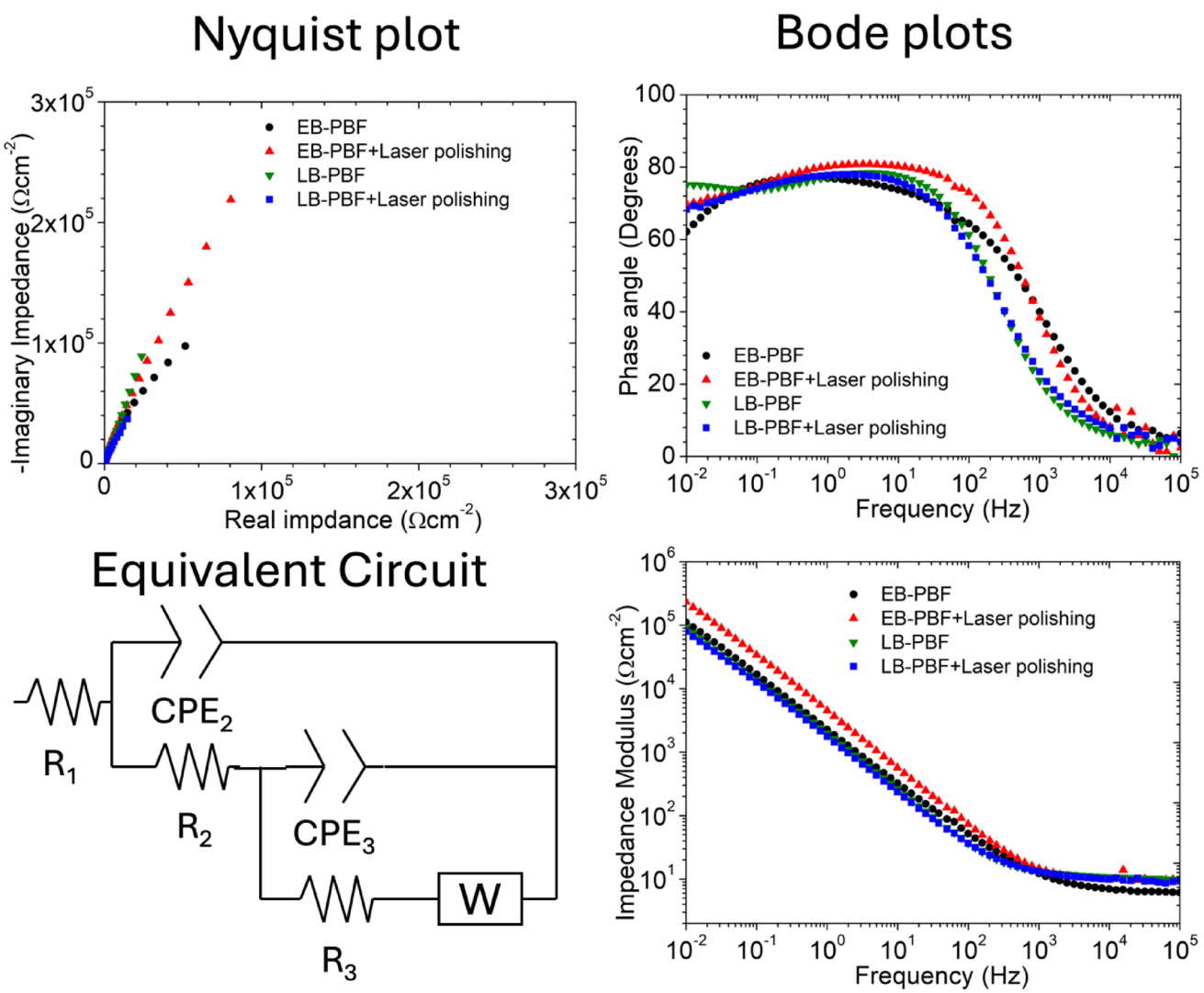

Fig. 7 Equivalent circuit, Bode and Nyquist plots of the samples at 1 h of immersion in SBF at 310 K and 7.4 pH

charge alignment on the oxide surface, while R_{film} reflects charge transfer resistance across the passive layer [61, 63–66]. These elements were connected in series with R_s.

A third time constant appeared at lower frequencies (10^{-1}–10^{1} Hz) as a change in slope and angle phase peak flattening in the Bode plots. This was represented by a second CPE–R pair assigned to the exposed metallic substrate beneath the passive film (CPE_{bared} and R_{bared}) [55, 62]. This contribution reflects metal oxidation and pit initiation sites.

At low frequencies, both the Bode and Nyquist plots exhibited a linear tail, consistent with Warburg impedance (W), indicating that mass transport and diffusion processes play a role in corrosion behaviour [61, 65, 67, 68]. This element was placed in series with R_{bared}. The diffusion process is attributed to both (i) surface roughness, which restricts electrolyte penetration, and (ii) defects in the passive film, such as pores or microcracks [15–17, 62, 63].

The final equivalent circuit (Fig. 7) is consistent with corrosion mechanisms reported for passive titanium alloys in simulated body fluids [61].

Table 5 summarises the fitted circuit parameters. The low χ^2 values ($\approx 10^{-4}$) demonstrate excellent agreement between the model and experimental data [51, 66, 69, 70]. The passive film capacitance (CPE_{film}) was similar across all samples, suggesting oxide films of comparable thickness, consistent with the proportional relationship between capacitance and film thickness [15, 16, 51, 60]. The CPE exponents (n_{film} and n_{bared}) ranged between 0.73 and 0.96, confirming non-ideal capacitive behaviour associated with surface roughness and oxide defects [71, 72].

Differences in Warburg impedance between polished and unpolished samples indicated variation in mass-transport processes. Notably, EB-PBF + laser polishing samples exhibited a shorter diffusion time, suggesting a reduced diffusion pathway length [68]. This improvement is attributed

Table 5 Equivalent circuit characteristics of the samples in the immersion of SBF at 310 K and 7.4 pH

Sample	R_s (Ω cm^2)	R_{film} (Ω cm^2)	CPE_{film} (S s^n cm^{-2}) (10^{-5})	n_{film}	R_{barc} (Ω cm^2) (10^5)	CPE_{bare} (S s^n cm^{-2}) (10^{-5})	n_{bare}	t (s$^{1/2}$)	W (Ss$^{0.5}$ cm^{-2}) (10^{-4})	R_{Total} (Ω cm^2) (10^5)	χ^2 (10^{-4})
EB-PBF	7.482±0.009	169±5	3.600±0.009	0.86±0.05	1.685±0.005	3.090±0.004	0.84±0.06	1.980 10^{-2}±9 10^{-5}	4.630±0.007	1.708±0.006	3.22±0.06
EB-PBF + laser polishing	9.361±0.008	24±6	7.480±0.006	0.83±0.06	2.419±0.007	1.060±0.004	0.96±0.05	3.869 10^{-4}±9 10^{-7}	0.619±0.006	2.581±0.009	3.65±0.05
LB-PBF	8.924±0.007	110±7	2.070±0.005	0.83±0.03	1.948±0.006	0.530±0.004	0.73±0.06	1.120 10^{-2}±7 10^{-5}	3.920±0.003	1.975±0.008	5.89±0.08
LB-PBF + laser polishing	9.822±0.006	8±4	3.680±0.007	0.88±0.02	1.532±0.008	7.010±0.009	0.86±0.05	∞	1.650±0.009	2.138±0.005	7.28±0.09

to the reduction of pores and microcracks by the laser process, which mitigates both geometric confinement of electrolyte transport and chloride-assisted passive film breakdown. For LB-PBF + laser polishing samples, an infinite diffusion time was used to obtain optimal fitting, which can reflect a more homogeneous surface and reduced mass transport limitations. Overall, diffusion characteristics were similar between manufacturing routes, with laser polishing producing the most visible improvements.

The total resistance of the samples (R_{Total}) was determined as the summation of the individual EIS resistances (R_{film}, R_{bared}, and 1/W), as detailed in Eq. (9) [66, 68].

$$R_{Total} = R_{film} + R_{bared} + W^{-1} \tag{9}$$

R_{Total} of the samples were consistent with their $C.R._{pass}$ (Sect. 3.2.2), as this parameter is directly associated with the passive film corrosion rate [66, 68].

It is noteworthy that these findigns delivers the first systematic characterisation of the corrosion mechanism of laser-polished EB-PBF and LB-PBF materials in the SBF environment.

4 Surface analysis after corrosion (PPC) test

Post-corrosion surface analyses revealed clear evidence of localised degradation mechanisms for all conditions, characterised by porous, cracked, and roughened regions associated with corrosion pits (Fig. 8). These features arise from the interaction between titanium oxides and aqueous ions, leading to a sequence of hydration reactions that transform amorphous TiO_2 into hydroxylated species [14, 66]:

$$TiO_2 + 2H_2O \leftrightarrow Ti(OH)_3{}^+ + OH^-$$

$$TiO_2 + 2H_2O \leftrightarrow TiO_2(OH)^- + H_3O^+$$

The formation of H_3O^+ and OH^- modifies local chemistry within pits, generating acid–base gradients that destabilise the oxide layer. Proton accumulation promotes hydrogen absorption and embrittlement of the Ti–6Al–4V alloy, contributing to brittle cracking [14, 66], whereas the formation of titanium hydroxides results in a porous, less protective surface morphology [66]. The presence of microcracks further accelerates electrolyte ingress, facilitating continued localised attack.

A second degradation pathway involves dissolution and re-precipitation of passive film species. Aggressive anions, predominantly chloride ions from SBF-react with titanium oxides to form soluble intermediates [14, 55, 73]. Due to their small ionic radius, chloride ions can diffuse through

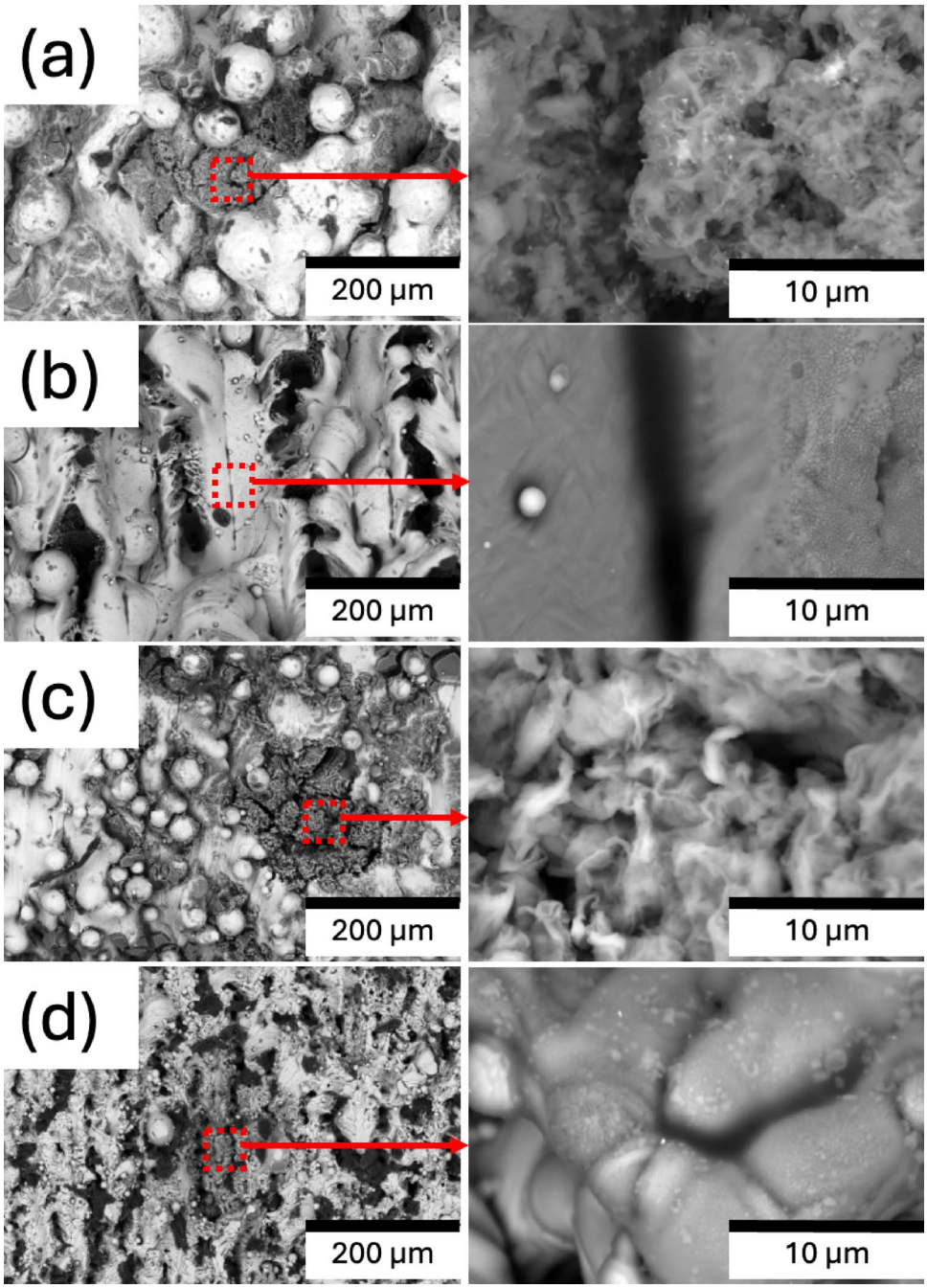

Fig. 8 SEM images with BSE of the **a** EB-PBF, **b** EB-PBF + laser polishing, **c** LB-PBF, and **d** LB-PBF + laser polishing corroded (after PPC) surface in SBF at 308 K and 7.4 pH

the passive layer, where they induce internal dissolution, pit nucleation, and porosity formation [55]. These mechanisms are consistent with the metastable pitting behaviour and current transients observed in AEN and PPC analyses (Sects. 3.2.1 and 3.2.2).

Notably, the morphology of corroded regions varied significantly between polished and unpolished samples. Laser-polished surfaces (Fig. 8b, d) exhibited fewer pores and cracks, and pits were more isolated and shallow compared to those on unpolished surfaces (Fig. 8a, c). This improvement reflects a more compact and defect-free passive film, formed on surfaces where laser polishing had removed powder agglomerates, reduced surface roughness, and altered near-surface microstructure. These modifications reduce the number of oxide vacancies and adsorption sites for chloride ions, thereby slowing their ingress and decreasing pit propagation kinetics. This observation is consistent with the higher E_{bp}, lower I_{pass}, and reduced diffusion impedance (W) observed for polished samples in PPC and EIS results.

EDS elemental mapping (Fig. 9) further supports these interpretations. All samples showed a local depletion of metallic elements (Ti, Al, V) within pits, accompanied by a

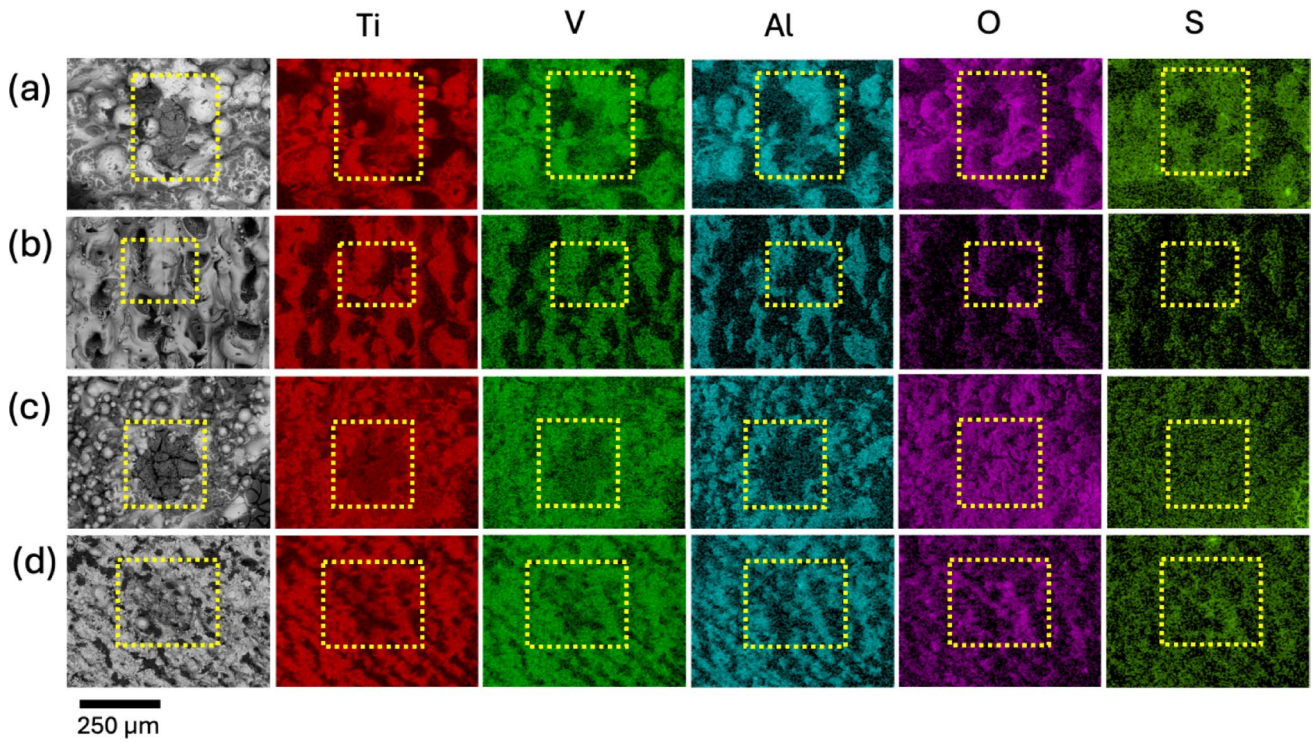

Fig. 9 EDS mapping analyses of the **a** EB-PBF, **b** EB-PBF + laser polishing, **c** LB-PBF, and **d** LB-PBF + laser polishing corroded (after PPC) surface in SBF at 310 K and 7.4 pH. The pitting is indicated with a yellow square

corresponding increase in oxygen concentration, attributed to repassivation of the exposed alloy surface. This agrees with PPC results, where reverse scans demonstrated spontaneous restoration of passivity following breakdown. The repassivated film is typically richer in hydroxylated species and therefore exhibits higher oxygen content than the native oxide [14, 66].

Interestingly, localised sulphur concentrations were detected across all samples, suggesting incorporation into the corrosion products during exposure. This phenomenon can originate from adsorption of sulphate species present in SBF, which can participate in passive film modification and potentially promote biointegration [15]. The persistence of sulphur after cleaning (Sect. 2.2) suggests strong surface affinity or chemical incorporation, although further work would be required to confirm its biological implications.

Overall, surface analyses after corrosion demonstrated that the laser polishing process reduces pit severity by enhancing passive film compactness and reducing defect density, but does not eliminate corrosive degradation entirely. These findings align with the electrochemical behaviour observed in previous sections: lower metastable activity (AEN), higher passive film breakdown potentials (PPC), and reduced diffusion impedance and shorter diffusion paths (EIS); confirming that the corrosion performance of AM Ti–6Al–4V is strongly surface-state-dependent and can be significantly improved through nanosecond laser polishing.

5 Conclusions

This study investigated the influence of infrared nanosecond pulsed laser polishing on the surface morphology and corrosion behaviour of Ti–6Al–4V manufactured using electron beam (EB-PBF) and laser-based (LB-PBF) powder bed fusion in simulated body fluid (SBF). The main findings are summarised below:

(1) Laser polishing substantially reduced surface roughness and removed surface defects from both AM processes. The elimination of adhered particles and sealing/opening of pores resulted in a measurable reduction in S_a for both materials, with EB-PBF showing the largest improvement due to its initially higher roughness. Laser polishing also altered crystallographic orientation, and in EB-PBF, induced local microstructural refinement attributable to longer remelting and re-solidification times.
(2) Laser polishing significantly enhanced the thermodynamic corrosion resistance of Ti–6Al–4V. The passive film breakdown potential (E_{bp}) increased from 1.661 V to 2.001 V in EB-PBF (ΔE 0.340 V) and from 1.800

V to 1.900 V in LB-PBF (ΔE 0.100 V), reflecting improved passive film stability. These improvements are attributed to (i) the reduction of surface asperities and crevices, which reduces chemically active sites, and (ii) more homogeneous grain orientations following polishing. The EB-PBF + laser polishing condition exhibited the highest E_{bp}, indicating the strongest resistance to passive film breakdown.

(3) Laser polishing process reduces the kinetic corrosion rate ($C.R._{pass}$) of Ti–6Al–4V by in 40% for LB-PBF samples (from 25 µm year^{-1} to 15 µm year^{-1}) and by 6.5fold for EB-PBF samples (72 µm year^{-1} to 11 µm year^{-1}). These improvements are linked to reduced true surface area exposure, fewer localised activation sites, and thicker, more uniform passive films.

(4) All samples exhibited the same corrosion mechanism, comprising (i) dissolution resistance (R_s), (ii) passive film response (CPE_{film}/R_{film}), (iii) bared metal response (CPE_{bared}/R_{bared}), and (iv) a diffusion impedance (W). Laser-polished samples demonstrated reduced diffusion impedance and shorter diffusion times, indicating less hindered transport of species through surface features, consistent with smoother surfaces and fewer microstructural defects.

(5) Post-corrosion surface analysis showed less severe porosity and cracking in laser-polished samples, confirming that the improved electrochemical behaviour corresponded to reduced pit propagation and increased passivity recovery. Despite comparable oxide compositions, laser-polished samples exhibited fewer defect sites available for chloride ion adsorption.

Overall, the nanosecond infrared laser polishing process has been demonstrated to be an effective, non-contact surface engineering method that improves both thermodynamic and kinetic corrosion resistance of AM Ti–6Al–4V without altering its alloy chemistry. This is particularly relevant for biomedical applications, as the observed reduction in corrosion rate for EB-PBF parts indicates potential extension of implant service life and improved in-vivo reliability. The process, therefore, offers a promising, scalable strategy for enhancing the performance of additively manufactured titanium components, especially those with complex geometries where conventional finishing is not feasible.

Notably, a rigorous quantitative analysis of grain size distribution and phase fraction is identified as an important direction for future work. Such analysis would require a systematic investigation under controlled experimental conditions, including targeted experimental design and advanced microstructural characterisation, which is beyond the scope of the present study.

Acknowledgements The author GAL would like to thank the CTI's Open Labs - Multiple Users and Shared Facilities from LAprint, CTI Renato Archer, research institution from MCTI.

Author contributions J.I. Ahuir-Torres and G.A. Longhitano developed the concept of the paper and wrote the manuscript . G.A. Longhitano fabricated the additively manufactured samples. J.I. Ahuir-Torres carried out the laser polishing, chemical composition and microstructural characterisation, and the electrochemical analyses. G. West conducted the analyses and images of the Figure 2. All authors reviewed the manuscript.

Data availability No datasets were generated or analysed during the current study.

Declarations

Competing interests The authors declare no competing interests.

References

1. Spetzger U, Frasca M, König SA (2016) Surgical planning, manufacturing and implantation of an individualized cervical fusion titanium cage using patient-specific data. Eur Spine J 25:2239–2246
2. Jardini AL, Larosa MA, de Carvalho Zavaglia CA, Bernardes LF, Lambert CS, Kharmandayan P, Calderoni D, Maciel Filho R (2014) Customised titanium implant fabricated in additive manufacturing for craniomaxillofacial surgery: this paper discusses the design and fabrication of a metallic implant for the reconstruction of a large cranial defect. Virtual Phys Prototyp 9(2):115–125
3. Qin M, Liu Y, Wang L, He J, Xuan M, Hua C, Li D, Jin Z, Wang X (2015) Design and optimization of the fixing plate for customized mandible implants. J Craniomaxillofac Surg 43(7):1296–1302
4. Facchini L, Magalini E, Robotti P, Molinari A, Höges S, Wissenbach K (2010) Ductility of a Ti–6Al–4V alloy produced by selective laser melting of prealloyed powders. Rapid Prototyp J 16(6):450–459
5. Longhitano GA, Machado LMR, Jardini AL, Baldin EK, Santos PB, Filho RM, Malfatti CdF, Zavaglia CAdC (2022) Fracture behavior under compression loading of surface-cleaned metallic lattice structures. Int J Adv Manuf Technol 121(5):3309–3321
6. Zhao B, Wang H, Qiao N, Wang C, Hu M (2017) Corrosion resistance characteristics of a Ti–6Al–4V alloy scaffold that is fabricated by electron beam melting and selective laser melting for implantation in vivo. Mater Sci Eng C Mater Biol Appl 70:832–841

7. Gisario A, Barletta M, Veniali F (2022) Laser polishing: a review of a constantly growing technology in the surface finishing of components made by additive manufacturing. Int J Adv Manuf Technol 120(3):1433–1472
8. De Damborenea J, Arenas M, Larosa MA, Jardini AL, de Carvalho-Zavaglia CA, Conde A (2017) Corrosion of Ti6Al4V pins produced by direct metal laser sintering. Appl Surf Sci 393:340–347
9. Rosa B, Mognol P, Hascoët J-Y (2015) Laser polishing of additive laser manufacturing surfaces. J Laser Appl 27: p S29102 https://doi.org/10.2351/1.4906385
10. Wang W, Yung K, Choy H, Xiao T, Cai Z (2018) Effects of laser polishing on surface microstructure and corrosion resistance of additive manufactured CoCr alloys. Appl Surf Sci 443:167–175
11. Perry TL, Werschmoeller D, Li X, Pfefferkorn FE, Duffie NA (2009) Pulsed laser polishing of micro-milled Ti6Al4V samples. J Manuf Process 11(2):74–81
12. Li J, Zuo D (2021) Laser polishing of additive manufactured Ti6Al4V alloy: a review. Opt Eng 60(2):020901–020901
13. Yung K, Xiao T, Choy H, Wang W, Cai Z (2018) Laser polishing of additive manufactured CoCr alloy components with complex surface geometry. J Mater Process Technol 262:53–64
14. Tamilselvi S, Raman V, Rajendran N (2006) Corrosion behaviour of Ti–6Al–7Nb and Ti–6Al–4V ELI alloys in the simulated body fluid solution by electrochemical impedance spectroscopy. Electrochim Acta 52(3):839–846
15. Ahuir-Torres J, Chadwick J, West G, Kotadia H, Öpöz T (2024) Effect of electrical discharge machining (EDM) bath composition on long-term corrosion of Ti–6Al–4V in simulated body fluid. Electrochim Acta 503:144865
16. Ahuir-Torres J, Kotadia H, Öpöz T (2023) Effect of the electrical discharge machining on Ti6Al4V corrosion behaviour in simulated body fluid. Surf Coat Technol 470:129830
17. Longhitano GA, García IM, Arenas MA, Damborenea JJde, Maciel Filho R, Conde A (2024) Effect of designed pore size on electrochemical, wear, and tribocorrosion behavior of additively manufactured Ti–6Al–4V lattice structures. Addit Manuf 79:103931
18. Fonseca EB, Gabriel AH, Rocha TM, Valim DB, Lopes ÉS (2025) A method to evaluate the processability of metallic alloys by laser-based powder bed fusion. Mater Today Commun 44:111806
19. Dawes J, Bowerman R, Trepleton R (2015) Introduction to the additive manufacturing powder metallurgy supply chain. Johnson Matthey Technol Rev 59(3):243–256
20. Körner C (2016) Additive manufacturing of metallic components by selective electron beam melting—a review. Int Mater Rev 61(5):361–377
21. Carolo LC (2022) A review on the influence of process variables on the surface roughness of Ti–6Al–4V by electron beam powder bed fusion. Addit Manuf 59:103103
22. Al-Mahdy A, Kotadia H, Sharp M, Opoz T, Mullett J, Ahuir-Torres J (2023) Effect of surface roughness on the surface texturing of 316 l stainless steel by nanosecond pulsed laser. Lasers Manuf Mater Process 10(1):141–164
23. Jaritngam P, Saetang V, Qi H, Dumkum C (2023) Surface polishing of additively manufactured Ti6Al4V titanium alloy by using a nanosecond pulse laser. Int J Adv Manuf Technol 127(7):3463–3480
24. Obeidi MA, McCarthy E, O'Connell B, Ul Ahad I, Brabazon D (2019) Laser polishing of additive manufactured 316L stainless steel synthesized by selective laser melting. Materials (Basel) 12(6):991
25. Joignant AN, Xi Y, Muddiman DC (2023) Impact of wavelength and spot size on laser depth of focus: considerations for mass spectrometry imaging of non-flat samples. J Mass Spectrom 58(5):e4914
26. Metelkova J, Kinds Y, Kempen K, de Formanoir C, Witvrouw A, Van Hooreweder B (2018) On the influence of laser defocusing in selective laser melting of 316L. Addit Manuf 23:161–169
27. Cao S, Zou Y, Lim CVS, Wu X (2021) Review of laser powder bed fusion (LPBF) fabricated Ti–6Al–4V: process, post-process treatment, microstructure, and property. Light Adv Manuf 2(3):313–332
28. Chern AH, Nandwana P, Yuan T, Kirka MM, Dehoff RR, Liaw PK, Duty CE (2019) A review on the fatigue behavior of Ti–6Al–4V fabricated by electron beam melting additive manufacturing. Int J Fatigue 119:173–184
29. Guan Y, Li Y, Wang H (2021) Laser polishing of additive-manufactured Ti alloys and Ni alloys. Additive manufacturing. Elsevier, pp 343–368
30. Zhihao F, Libin L, Longfei C, Yingchun G (2018) Laser polishing of additive manufactured superalloy. Procedia CIRP 71:150–154
31. Longhitano GA, Larosa MA, Jardini AL, de Carvalho Zavaglia CA, Ierardi MCF (2018) Correlation between microstructures and mechanical properties under tensile and compression tests of heat-treated Ti–6Al–4V ELI alloy produced by additive manufacturing for biomedical applications. J Mater Process Technol 252:202–210
32. Mustafa H, Mezera M, Matthews DTA, Römer G (2019) Effect of surface roughness on the ultrashort pulsed laser ablation fluence threshold of zinc and steel. Appl Surf Sci 488:10–21
33. Dinesh Babu P, Balasubramanian K, Buvanashekaran G (2011) Laser surface hardening: a review. Int J Surf Sci Eng 5(2–3):131–151
34. Eberle G, Schmidt M, Pude F, Wegener K (2016) Laser surface and subsurface modification of sapphire using femtosecond pulses. Appl Surf Sci 378:504–512
35. Szyszko W (1995) Melting and diffusion under nanosecond laser pulse. Appl Surf Sci 90(3):325–331
36. Vadali M, Ma C, Duffie NA, Li X, Pfefferkorn FE (2012) Pulsed laser micro polishing: surface prediction model. J Manuf Process 14(3):307–315
37. Liu J, Zhao K, Wang X, Li H (2024) Effect of initial surface morphology and laser parameters on the laser polishing of stainless steel manufactured by laser powder bed fusion. Materials (Basel) 17(20):4968
38. Bhaduri D, Penchev P, Batal A, Dimov S, Soo SL, Sten S, Harrysson U, Zhang Z, Dong H (2017) Laser polishing of 3D printed mesoscale components. Appl Surf Sci 405:29–46
39. Wang X, Chou K (2018) EBSD study of beam speed effects on Ti–6Al–4V alloy by powder bed electron beam additive manufacturing. J Alloys Compd 748:236–244
40. Chen J, Fabijanic D, Zhang T, Lui E, Brandt M, Xu W (2022) Deciphering the transformation pathway in laser powder-bed fusion additive manufacturing of Ti–6Al–4V alloy. Addit Manuf 58:103041
41. Miescher I, Rieber J, Schweizer TA, Orlietti M, Tarnutzer A, Andreoni F, Meier Buergisser G, Giovanoli P, Calcagni M, Snedeker JG (2024) In vitro assessment of bacterial adhesion and biofilm formation on novel bioactive, biodegradable electrospun fiber meshes intended to support tendon rupture repair. ACS Appl Mater Interfaces 16(5):6348–6355
42. Jäger M, Jennissen HP, Dittrich F, Fischer A, Köhling HL (2017) Antimicrobial and osseointegration properties of nanostructured titanium orthopaedic implants. Materials 10(11):1302
43. Kök HI, Andreeva T, Stammkötter S, Reinholdt C, Akbas O, Jahn A, Gamon F, Fuest S, Teschke M, Schäfer M (2025) Characterization and modeling of additively manufactured Ti–6Al–4V alloy with modified surfaces for medical applications. Front Bioeng Biotechnol 13:1526873

44. Jiang Z, Norby T, Middleton H (2010) Evaluation of metastable pitting on titanium by charge integration of current transients. Corros Sci 52(10):3158–3161
45. Cui Y-W, Chen L-Y, Qin P, Li R, Zang Q, Peng J, Zhang L, Lu S, Wang L, Zhang L-C (2022) Metastable pitting corrosion behavior of laser powder bed fusion produced Ti–6Al–4V in Hank's solution. Corros Sci 203:110333
46. Kelly RG, Scully JR, Shoesmith D, Buchheit RG (2002) Electrochemical techniques in corrosion science and engineering. CRC Press
47. Mansfeld F, Sun Z (1999) Localization index obtained from electrochemical noise analysis. Corrosion 55(10):915–918
48. Souza ECd, Rossitti SM, Fortulan CA, Rollo JMDdA (2016) Influence of ferrite phase content on the electrochemical properties of duplex stainless steels. Mater Res 20(1):21–29
49. Toloei A, Stoilov V, Northwood D (2013) The relationship between surface roughness and corrosion, ASME International mechanical engineering congress and exposition. American Society of Mechanical Engineers, p V02BT02A054.
50. Esmailzadeh S, Aliofkhazraei M, Sarlak H (2018) Interpretation of cyclic potentiodynamic polarization test results for study of corrosion behavior of metals: a review. Prot Met Phys Chem Surf 54:976–989
51. de Assis SL, Wolynec S, Costa I (2006) Corrosion characterization of titanium alloys by electrochemical techniques. Electrochim Acta 51(8–9):1815–1819
52. Yi G, Liu X, Zheng C, Zhang H, Xu C, Cui Y-W, Liu S (2021) Characteristics of passive films formed on as-cast Ti–6Al-4V in Hank's solution before and after transpassivation. Front Mater 7:640081
53. Davepon B, Schultze J, König U, Rosenkranz C (2003) Crystallographic orientation of single grains of polycrystalline titanium and their influence on electrochemical processes. Surf Coat Tech 169:85–90
54. Sander G, Thomas S, Cruz V, Jurg M, Birbilis N, Gao X, Brameld M, Hutchinson C (2017) On the corrosion and metastable pitting characteristics of 316L stainless steel produced by selective laser melting. J Electrochem Soc 164(6):C250
55. Sharma A, Oh MC, Kim J-T, Srivastava AK, Ahn B (2020) Investigation of electrochemical corrosion behavior of additive manufactured Ti–6Al–4V alloy for medical implants in different electrolytes. J Alloys Compd 830:154620
56. Martin É, Azzi M, Salishchev G, Szpunar J (2010) Influence of microstructure and texture on the corrosion and tribocorrosion behavior of Ti–6Al–4V. Tribol Int 43(5–6):918–924
57. Garbacz H, Królikowski A (2019) Corrosion resistance of nanocrystalline titanium. Nanocrystalline titanium. Elsevier, pp 145–173
58. Ahuir-Torres JI, Jabar S, Franciosa P, Ceglarek D, Kotadia HR (2024) The microstructure-corrosion relationships in laser-welded dissimilar steel-to-aluminium joints. NPJ Mater Degrad 8(1):105
59. Ahuir-Torres JI, Yang X, West G, Kotadia HR (2024) Corrosion behaviour of SiC particulate reinforced AZ31 magnesium matrix composite in 3.5% NaCl with and without heat treatment. Mater Chem Phys 320:129467
60. McCafferty E (2010) Introduction to corrosion science. Springer
61. Bocchetta P, Chen L-Y, Tardelli JDC, Reis ACd, Almeraya-Calderón F, Leo P (2021) Passive layers and corrosion resistance of biomedical Ti–6Al–4V and β-Ti alloys. Coatings 11(5):487
62. Hwang I-J, Choe H-C, Brantley WA (2017) Electrochemical characteristics of Ti–6Al–4V after plasma electrolytic oxidation in solutions containing Ca, P, and Zn ions. Surf Coat Technol 320:458–466
63. Leksycki K, Kaczmarek-Pawelska A, Ochał K, Gradzik A, Pimenov DY, Giasin K, Chuchala D, Wojciechowski S (2021) Corrosion resistance and surface bioactivity of Ti6Al4V alloy after finish turning under ecological cutting conditions. Materials (Basel) 14(22):6917
64. Harrington DA, Van Den Driessche P (2011) Mechanism and equivalent circuits in electrochemical impedance spectroscopy. Electrochim Acta 56(23):8005–8013
65. Ciucci F (2019) Modeling electrochemical impedance spectroscopy. Curr Opin Electrochem 13:132–139
66. Qin X, Yang H, Zhao Y, Wan S, Zhao X, Yu T, Wang X, Zhang Z (2024) Investigation of the microstructural characteristics of laser-cladded Ti6Al4V titanium alloy and its corrosion behavior in simulated body fluid. Mater Today Commun 41:110780
67. Navarro-Laboulais J, García-Jareño J, Vicente F (2002) Kramers–Kronig transformation, dc behaviour and steady state response of the Warburg impedance for a disk electrode inlaid in an insulating surface. J Electroanal Chem 536(1–2):11–18
68. Moya A (2024) Low-frequency approximations to the finite-length Warburg diffusion impedance: the reflexive case. J Energy Storage 97:112911
69. Pathote D, Jaiswal D, Singh V, Behera C (2022) Optimization of electrochemical corrosion behavior of 316L stainless steel as an effective biomaterial for orthopedic applications. Mater Today Proc 57:265–269
70. Quevedo MC, Galicia G, Mayen-Mondragon R, Llongueras JG (2018) Role of turbulent flow seawater in the corrosion enhancement of an Al–Zn–Mg alloy: an electrochemical impedance spectroscopy (EIS) analysis of oxygen reduction reaction (ORR). J Mater Res Technol 7(2):149–157
71. Chen X, Liao Q, Gong M, Fu Q (2023) Corrosion performances of selective laser melting Ti6Al4V alloy in different solutions. Metals (Basel) 13(2):192
72. Alves V, Reis R, Santos I, Souza D, Gonçalves TdF, Pereira-da-Silva M, Rossi A, Da Silva L (2009) In situ impedance spectroscopy study of the electrochemical corrosion of Ti and Ti–6Al–4V in simulated body fluid at 25 C and 37 C. Corros Sci 51(10):2473–2482
73. El Hadad AA, Peón E, García-Galván FR, Barranco V, Parra J, Jiménez-Morales A, Galván JC (2017) Biocompatibility and corrosion protection behaviour of hydroxyapatite sol-gel-derived coatings on Ti6Al4V alloy. Materials (Basel) 10(2):94